Nonlinear and ultrafast effects

8

Maxim Shcherbakov[a,b], *Sheng Liu*[c], *Igal Brener*[c,d], *Andrey Fedyanin*[b]
[a]School of Applied and Engineering Physics, Cornell University, Ithaca, NY, United States, [b]Faculty of Physics, Lomonosov Moscow State University, Moscow, Russia, [c]Sandia National Laboratories, Albuquerque, NM, United Sates, [d]Center for Integrated Nanotechnologies, Sandia National Laboratories, Albuquerque, NM, United States

8.1 Introduction

In 1961, a mere year after the first laser was invented, the world witnessed the birth of nonlinear optics (NLO), when the second harmonic was observed in a nonlinear crystal [1]. Fast forward more than 50 years, and NLO phenomena are abundant and found anywhere from research laboratories to data centers and manufacturing. Examples of commercially available systems that operate via NLO processes are ultrashort-pulse lasers used in surgery and other biomedical applications, multiphoton microscopes, fiber amplifiers and repeaters for optical telecommunications, tunable parametric oscillators and other light sources such as the green laser pointer. Despite the success of NLO, a well-acknowledged limitation of its processes is their inherently low efficiency requiring macroscopic volumes of materials for light-light interaction. This limitation prohibits scalability of NLO to the nanoscale. Finding routes to enhanced optical nonlinearities has been a subject of intense research for the past several decades.

The main approach to enhanced nonlinearities at the nanoscale consists on finding paths to increased light confinement. Nanostructures with surface plasmons, like metal films, nanoantennas, gratings and metamaterials, do an excellent job of localizing light to subwavelength volumes, yielding enhanced generation of optical harmonics [2], all-optical switching [3], and other nonlinearities [4]. Light confinement in plasmonic nanostructures suffers from the drawback of increased optical losses, which hinders conversion efficiencies and thus limits the application scope of these materials for NLO. A different approach to light confinement has recently been developed using all-dielectric nanostructures [5,6], a paradigm in nanophotonics that is the main topic of this book. Nanostructured materials with high refractive indices ($n > 2$) can provide ultrastrong light confinement through Mie resonant modes [7], as well as provide venues for light wavefront and polarization control (and other exciting properties), as explored in other chapters of this book. One of the obvious advantages of using dielectrics as the constituent materials is their resilience to high-power laser radiation; this property serves as one of the main motivations for the work reviewed in this chapter. In this chapter, we survey experimental studies of how strong laser pulses interact with all-dielectric Mie resonators and metasurfaces. The chapter is organized as follows. In Section 8.2, we briefly recall the basics of nonlinear light–matter interaction, providing a classical, phenomenological description of optical nonlinearities reviewed in this chapter. Section 8.3 discusses nonlinear all-dielectric metaatoms and

Dielectric Metamaterials. https://doi.org/10.1016/B978-0-08-102403-4.00013-X

metasurfaces: methods of fabrication, typical measurement techniques, and results in generation of optical harmonics and other frequency-mixing phenomena, nonlinear refraction and effects under ultrastrong excitation. Section 8.4 showcases ultrafast phenomena in semiconductor-based metasurfaces, including instantaneous and free-carrier-related responses. Section 8.5 concludes the chapter, outlining future research directions within the young and exciting field of nonlinear all-dielectric metamaterials.

8.2 Basics of nonlinear optics

Nonlinear optics describes the interaction of intense laser light with matter, e.g., dielectrics or semiconductors. In this section, we provide just the basic expressions that highlight the rich nature of the NLO effects; we refer the reader to the excellent textbook material should they find themselves interested in further details [8,9].

In linear optics, the polarization $\mathbf{P}^{\mathrm{L}}$ induced by the external electromagnetic field with the electric-field vector $\mathbf{E}$:

$$\mathbf{P}^{\mathrm{L}} = \epsilon_0 \chi^{(1)} \cdot \mathbf{E}, \tag{8.1}$$

where $\chi^{(1)}$ is the linear susceptibility tensor of the material and the dot symbols denotes the inner tensor product. Under strong illumination, a nonlinear electric polarization $\mathbf{P}^{\mathrm{NL}}$ is induced in materials: $\mathbf{P}^{\mathrm{tot}} = \mathbf{P}^{\mathrm{L}} + \mathbf{P}^{\mathrm{NL}}$. This polarization is a nonlinear function of the fundamental beam electric-field strength $\mathbf{E}$, and can be represented as a series:

$$\mathbf{P}^{\mathrm{NL}} = \mathbf{P}^{(2)} + \mathbf{P}^{(3)} + \ldots \quad . \tag{8.2}$$

This series is a Taylor expansion over the small parameter $\mathbf{P}^{(i)} \approx (E/E_{\mathrm{at}})^i$, where $E_{\mathrm{at}} \approx 5 \cdot 10^{11}$ V/m is the atomic scale of the electric-field strength:

$$\mathbf{P}^{\mathrm{NL}} = \epsilon_0 [\chi^{(2)} : \mathbf{EE} + \chi^{(3)} \vdots \mathbf{EEE} + \ldots]. \tag{8.3}$$

Here, $\chi^{(i)}$ are the ith-order susceptibilities of the material, which are $(i+1)$st-rank tensors. The leading terms in this series are the second- and the third-order terms:

$$\mathbf{P}^{(2)}(\omega_1) = \epsilon_0 \chi^{(2)}(\omega_1; \omega_2, \omega_3) : \mathbf{E}_{\omega_2} \mathbf{E}_{\omega_3}, \tag{8.4}$$

$$\mathbf{P}^{(3)}(\omega_1) = \epsilon_0 \chi^{(3)}(\omega_1; \omega_2, \omega_3, \omega_4) \vdots \mathbf{E}_{\omega_2} \mathbf{E}_{\omega_3} \mathbf{E}_{\omega_4}. \tag{8.5}$$

Here, ω_i are the frequencies of the pump fields and the polarization induced in the material. Importantly and as seen from these expressions, the nonlinear polarization can mix external fields at different frequencies. The key observation here is that the polarization of materials under strong illumination contains terms oscillating at frequencies that are different from the frequencies of the incident fields $\mathbf{E}_{\omega_i}$. Such frequency conversion is a staple of NLO that is widely used in photonics.

Various NLO phenomena can be observed, depending on the frequencies of the interacting pump and nonlinear response fields. The simplest NLO effect based on the quadratic susceptibility $\chi^{(2)}$ is second-harmonic generation (SHG) that manifests itself as radiation at the doubled pump laser frequency: $\mathbf{P}^{(2)}(2\omega) = \epsilon_0 \chi^{(2)}(2\omega; \omega, \omega) : \mathbf{E}_\omega \mathbf{E}_\omega$. Other $\chi^{(2)}$ effects include optical rectification as a static electric field is induced in the nonlinear media, difference frequency generation, which is now very popular for generation of electromagnetic fields in the mid-infrared and THz frequency ranges, and sum frequency generation. Note that the quadratic susceptibility is a third-rank tensor. Due to symmetry considerations in centrosymmetric media, its components are equal to zero; furthermore, all the NLO effects governed by quadratic susceptibilities are small. Four-wave processes, whereby four electromagnetic waves exchange energy within the nonlinear material through Eq. (8.5), are based on the third-order nonlinear susceptibility, $\chi^{(3)}$. Typically, these processes can be observed in all materials, regardless of the material symmetry. Most notably, the frequency-degenerate case when three photons of the same frequency merge to create a photon of a tripled frequency corresponds to third-harmonic generation (THG): $\mathbf{P}^{(3)}(3\omega) = \epsilon_0 \chi^{(3)}(3\omega; \omega, \omega, \omega) \vdots \mathbf{E}_\omega \mathbf{E}_\omega \mathbf{E}_\omega$. Other nonlinear processes covered in this chapter are four-wave mixing, nonlinear refraction and nonlinear absorption, as well as higher-order frequency-mixing processes that utilize $\chi^{(i)}$, where $i > 3$.

On a final note, it is important to point out the importance of the electromagnetic field strength in the magnitude of $\mathbf{P}^{(i)}$, as locally enhanced electromagnetic fields can significantly boost the efficiencies of the nonlinear processes. Creating resonant response and enhanced localized fields is key to efficient nonlinearities in nanostructures, as shown throughout this chapter.

8.3 Nonlinear optics in Mie-resonant nanostructures

Enhancement of optical nonlinearities by nanostructures dates back to the 1970s when it was realized that the local fields that give rise to the nonlinear polarization in Eq. (8.3) can be enhanced by propagating surface plasmons [10] or localized surface plasmons [11] in noble metal films. In spite of the vast body of research on nonlinear plasmonic nanostructures [4], their applicability has been limited by low efficiencies, high Ohmic losses and low damage thresholds. Semiconductor-based nanostructures for nonlinear optics were introduced later [12,13]. They, in contrast with the main topic of the current Chapter, did not utilize enhancement of nonlinearities by electromagnetic modes but rather by resonant transitions occurring in quantum-confined systems. While the latter provide very strong NLO response through large nonlinear susceptibilities, they suffer from saturation effects and are limited to the mid-infrared spectrum range. Photonic crystals were one of the first patterned materials to have been suggested for strong NLO response via engineered electromagnetic wave propagation [14–17].

An approach for enhanced NLO effects utilizing strongly localized Mie-type resonances of nanoparticles emerged later, when it was realized that subwavelength

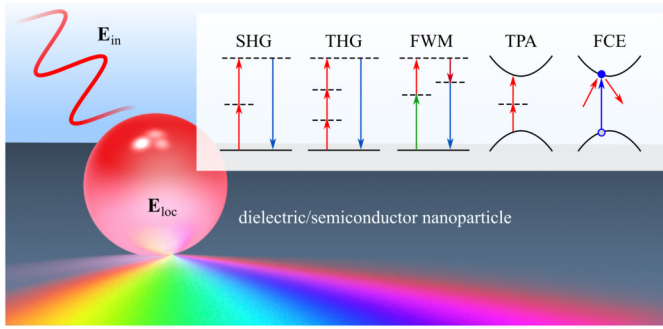

Figure 8.1 Illustration of resonantly enhanced nonlinear-optical processes in all-dielectric/semiconductor nanoparticles. Some of the processes covered in this chapter are second-harmonic generation (SHG), third-harmonic generation (THG), four-wave mixing (FWM), two-photon absorption (TPA), and free-carrier effects (FCE).

particles of high-index materials, e.g., silicon, can resonantly scatter light in the visible and IR [18–20]. For a simple geometry, such as a nanosphere, its localized fields are described by electromagnetic eigenmodes that can be expressed analytically:

$$\mathbf{E}_{\text{loc}} = E_{\text{in}} \sum_{n=1}^{\infty} i^n \frac{2n+1}{n(n+1)} \left(c_n \mathbf{M}_{o1n}^{(1)} - i d_n \mathbf{N}_{e1n}^{(1)} \right), \tag{8.6}$$

where E_{in} is the amplitude of the incident field, $\mathbf{M}_{o1n}^{(1)}$, and $\mathbf{N}_{e1n}^{(1)}$ are vector spherical harmonics (see [21], p. 95 for detailed expressions), and c_n and d_n are coefficients defined by [21], p. 100 (see also Chapter 3 of this book):

$$c_n = \frac{j_n(x)[x h_n^{(1)}(x)]' - h_n^{(1)}(x)[x j_n(x)]'}{j_n(mx)[x h_n^{(1)}(x)]' - h_n^{(1)}(x)[mx j_n(mx)]'}, \tag{8.7}$$

$$d_n = \frac{m j_n(x)[x h_n^{(1)}(x)]' - m h_n^{(1)}(x)[x j_n(x)]'}{m^2 j_n(mx)[x h_n^{(1)}(x)]' - h_n^{(1)}(x)[mx j_n(mx)]'}. \tag{8.8}$$

Here, $j_n(x)$ is the first-kind spherical Bessel function, $h_n^{(1)}(x)$ is the first-kind spherical Hankel function, $x = kr$ is the size parameter, k is the wavevector inside the sphere, r is the radius of the sphere, and m is the relative refractive index of the sphere. The magnetic permeability of the sphere is 1. Note that these are expressions for *internal* fields, as opposed to those used in problems involving scattering from a sphere.

An example of volume integrated local fields of a sphere is given in Fig. 8.2 for a set of refractive indices n_0 from 1.5 to 3.5. For all the spectra, the condition of the particle having a subwavelength dimension (compared to the free-space wavelength), $\lambda > 2r$, is met. Here, the role of the magnetic eigenmodes is apparent: for the wavelengths corresponding to the magnetic dipole mode (near $\lambda/n_0 = 0.85$) and the magnetic quadrupole mode (near $\lambda/n_0 = 0.6$), a considerable overall enhancement of the local electric field is obtained. In contrast, in the wavelength region of

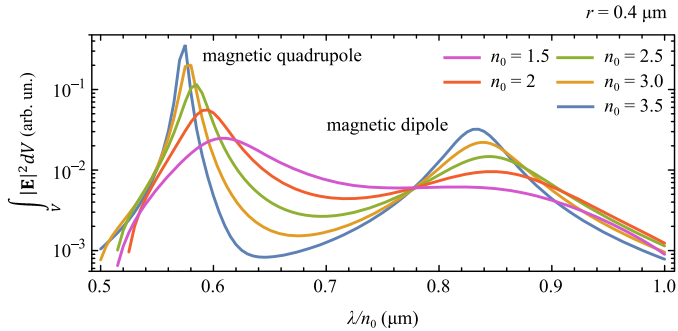

Figure 8.2 Integrated local fields inside a dielectric sphere with a refractive index of n and a radius of $r = 400$ nm, calculated using Eq. (8.6). The spectral region was chosen so that it captures the magnetic dipolar, magnetic quadrupolar resonances (indicated) and the electric-dipolar resonance (not apparent on the plots). For all spectra, the condition $\lambda > 2r$ is met.

the electric-dipole resonance, around $\lambda/n_0 = 0.65 - 0.8$, the enhancement is much less pronounced. These simplistic calculations give a clear indication of the role of the magnetic-type modes in the NLO response of Mie-resonant nanoparticles. The local fields within the nanoparticles $\mathbf{E}_{\text{loc}}$ that are supported by Mie-type modes can significantly enhance the nonlinear polarizability given by Eq. (8.3), giving rise to various frequency conversion processes and all-optical modulation schemes, as illustrated in Fig. 8.1.

8.3.1 Fabrication techniques

Here, we briefly outline the main methods to fabricate the nonlinear all-dielectric Mie-resonant nanostructures and metasurfaces. As shown in Fig. 8.3, the fabrication of the dielectric resonators shares common processing steps despite the variety of materials employed for studying NLO phenomena. The fabrication starts from a thin layer of a high refractive index material with a thickness of the order of λ/n_0; the exact thickness is determined by full-wave simulations of the particular design that is being implemented. Thin films of crystalline silicon are widely available as silicon-on-insulator (SOI) wafers with a SiO_2 under layers of a few microns followed by a Si substrate. However, the high refractive index contrast between the SiO_2 and the Si substrate inevitably produces undesired spectral interference [36]. Alternatively, to eliminate the interference, Si thin films can be directly deposited on low refractive index substrates [37,25,38–40]. Utilizing different deposition techniques, such as low pressure chemical vapor deposition or plasma enhanced chemical vapor deposition, either polycrystalline or amorphous Si thin films with desired thicknesses can be achieved. As an alternative, amorphous germanium can be used. Note that different Si crystal structures correspond to various refractive indices, bandgap and nonlinear coefficients. Different from group IV semiconductors, III–V semiconductors (such as GaAs) thin films are typically grown by metal-organic chemical vapor deposition (MOCVD) or molecular beam epitaxy (MBE) on lattice matched III–V substrates.

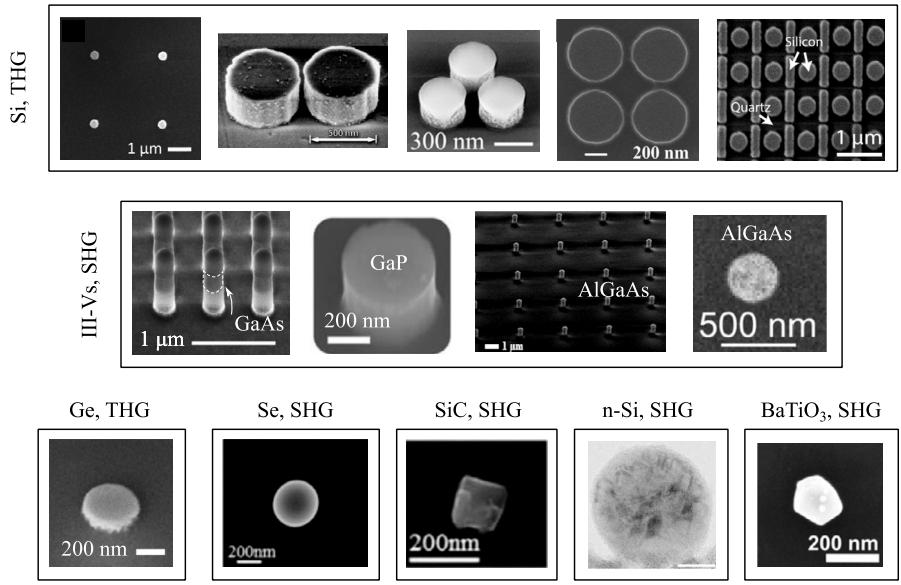

Figure 8.3 Designs of all-dielectric nanostructures for frequency conversion. Top row (Si-based), left to right: individual nanoparticles [22], dimers [23], trimers [24], quadrumers [25] and metasurfaces [26] for third-harmonic generation enhancement. Middle row (III–V-based), left to right: GaAs metasurfaces [27], GaP nanoparticles [28] and AlGaAs nanoparticles [29,30]. Bottom row, left to right (miscellaneous): Ge nanoparticles [31], Se nanoparticles [32], SiC nanoparticles [33], nanocrystalline Si nanoparticles [34], and perovskite nanoparticles [35]. Reprinted with permission from the corresponding sources. Third figure in the middle row reprinted with permission from V.F. Gili, L. Carletti, A. Locatelli, D. Rocco, M. Finazzi, L. Ghirardini, I. Favero, C. Gomez, A. Lemaître, M. Celebrano, C. De Angelis, G. Leo, Monolithic AlGaAs second-harmonic nanoantennas, Opt. Express 24 (2016) 15965, Optical Society of America.

Following the thin film growth, electron-beam lithography is often used to define etch masks. Electron-beam resists are chosen for high etching selectivity between the resists and the resonator materials. For example, negative-tone resist NEB-31A is often used for Si-based dielectric resonators, and HSQ (hydrogen silsesquioxane) can be used for III–V semiconductors. Next, inductively coupled plasma etch is typically used to transfer the shape of etch mask onto the semiconductor thin film for dielectric resonator formation. Variations of the ideal recipe are typically required because the plasma etch determines the resonator sidewall slope angle and roughness. Next, removing the etch mask can be optional depending on the purpose of the experiment and the refractive index of the mask. Finally, if the resonators are placed on top of a high-index substrate, either transferring them to a low-index substrate or oxidizing the high-index materials to their low index oxide is required [41].

8.3.2 Measurement apparatuses

Below, we briefly summarize the main principles of measurements that characterize the NLO response of the nanostructures described in this chapter.

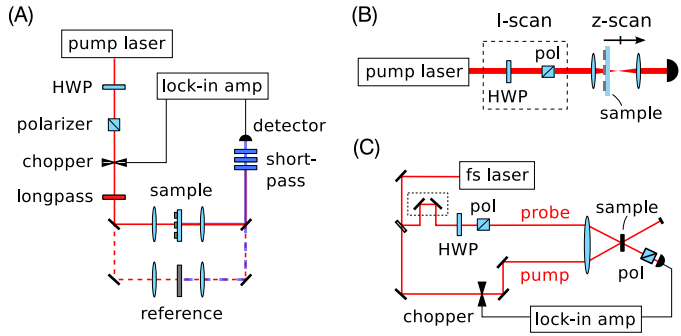

Figure 8.4 Typical experimental setups to study optical nonlinearities of nanostructures. (A) Harmonics generation spectroscopy setup. (B) Z-scan and I-scan setup. (C) Frequency-degenerate pump–probe setup.

8.3.2.1 Harmonic generation

A typical setup for harmonics generation spectroscopy is provided in Fig. 8.4, as adapted from earlier work [42,43]. A pulsed laser source is used as the pump beam. It is desirable to employ a wavelength-tunable pump so as to cover both resonant and non-resonant regimes of harmonics generation. Here, the pump beam is modulated by an optical chopper at a frequency of several kHz and focused by an aspheric lens to a beam waist of about 10 μm in diameter, leading to a maximum peak intensity spanning from $I = 1$ GW/cm^2 to 100 GW/cm^2. The generated harmonic radiation is collected and filtered out from the pump by a set of optical filters. The collimated harmonic radiation is directed to the cathode of a photomultiplier tube assembly or avalanche photodiode, in the case of a weak signal, or to a regular semiconductor photodetector if the signal is strong enough. The output of the detector is analyzed with a lock-in amplifier. Typically, the power dependence of the signal on the pump power is used as an indication that the signal arises from harmonic generation: $I_{n\omega} \propto I^n_{\text{pump}}$. If the harmonic generation process is efficient enough, its spectra can be measured directly with a spectrometer. Polarization of the pump beam can be controlled by a polarizer. Analyzing the harmonic radiation with an analyzer placed after the sample can reveal the structure of the nonlinear susceptibility tensor. Transmittance, reflectance and scattered-signal schemes have been successfully used for more detailed studies [44, 45,23,46].

8.3.2.2 Z-scan, I-scan

Techniques of z-scan and intensity scan (I-scan) are routinely used to determine the third-order nonlinear susceptibilities of materials, both their real and the imaginary parts [47]. While studying the real part of $\chi^{(3)}$ requires thick samples and cannot be readily applicable to ultrathin materials like metasurfaces, $\text{Im}\chi^{(3)}$ has been reported in a number of references; we will discuss those in Section 8.3.4. A typical setup for z-scan and I-scan measurements is shown in Fig. 8.4B.

8.3.2.3 Pump–probe spectroscopy

When a strong ultrashort laser pulse impinges on a solid-state medium, the state of the material can get strongly modified. If these modifications are reversible and consistent from pulse to pulse, then a technique called pump–probe spectroscopy can be used to study the transient optical properties caused by the pulses. A typical implementation of pump–probe spectroscopy is given in Fig. 8.4C. A train of femtosecond laser pulses is split into two: a stronger pump and a weaker probe. In order to remove unwanted pump scattering towards the detector, the polarization states of the beams are chosen to be orthogonal. The beams are focused onto the sample surface, and the intensity of the probe beam is then measured as a function of the delay between the pump and the probe. Pump–probe measurements are a powerful tool to characterize the strength of how light interacts with light through matter, and the lifetimes of the processes involved.

8.3.3 Harmonics generation and frequency mixing

In this section, we review recent experimental efforts to tailor harmonic generation from all-dielectric nanostructures. The subsections will address frequency conversion processes of different nonlinear orders, their conversion efficiencies and enhancement by Mie-type resonances, polarization properties and the roles of the nonlinear susceptibility tensor structure.

8.3.3.1 Second-harmonic generation

The most common materials for all-dielectric nanophotonics, such as silicon, germanium, titanium dioxide and many others, are centrosymmetric. This property makes detection of second-order nonlinear effects, such as second-harmonic generation (SHG), challenging. It was not until metasurfaces made from noncentrosymmetric materials (such as III–V-semiconductors) were developed [41,30,48] that SHG was observed in all-dielectric Mie-resonant structures. Earlier manifestations of size-dependent SHG from nanostructured semiconductors was observed in arrays of GaP nanowires [49], although the role of the nanowire eigenmodes was not emphasized. The first demonstration of SHG by magnetic Mie-type resonances in GaAs nanoparticles was reported later [44,27] and revealed four orders of magnitude enhancement with respect to an unstructured GaAs substrate and a conversion efficiency of $\eta_{2\omega} \approx 2 \times 10^{-5}$, see Fig. 8.5A. Conversion efficiency is defined as the intensity of the incoming pump beam divided by the intensity of the generated harmonic beam: $\eta_{2\omega} = I_{2\omega}/I_{\omega}$. This figure was further improved [27,30,50,51,28,52], resulting in $\eta_{2\omega} \approx 10^{-4}$ in AlGaAs nanostructures [53].

The zinc blende crystal structure of most III–V semiconductors defines a particular $\chi^{(2)}$ tensor where $\chi^{(2)}_{ijk} \neq 0$ only for $i \neq j \neq k$. As a consequence, SHG emitted from nanostructures based on III–V semiconductors has certain polarization and scattering properties. For a bulk GaAs wafer with two out of three crystallographic axes lying within the wafer's surface (x and y), no SHG will be observed at normal incidence.

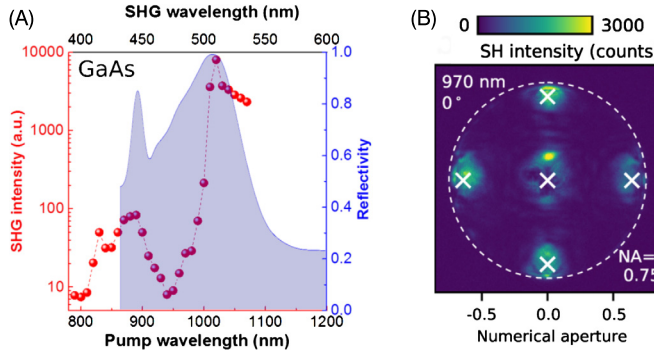

Figure 8.5 Second-harmonic generation in GaAs metasurfaces. (A) Enhancement of the second-harmonic output at the magnetic Mie-type resonance excited by pump pulses at $\lambda \approx 1000$ nm. Reproduced with permission from [27]. (B) Second-harmonic diffraction from a metasurface excited at a dark mode. Diffraction at an angle of close to 0°, which is forbidden in bulk GaAs, is observed. Reproduced with permission from [46].

The only nonlinear polarization will be generated along z: $P_z = 2\chi^{(2)}_{zyx} E_x E_y$, and it will not create a radiating field along z. However, fabricating an array of Mie-resonant nanopartices (nanodisks) out of such a wafer, will allow efficient far-field SHG for two reasons [46]. First, if the period of the array is larger than the SHG wavelength, the diffraction pattern will utilize the P_z polarization, giving rise to detectable diffraction orders. Second, the certain Mie-type resonances will support local fields along the z direction, creating SH polarizability along x or y, thus enabling the previously-forbidden normally-emitting SHG, see Fig. 8.5B. Other implications of the nontrivial III–V tensor structure are the polarization properties of the SHG radiation itself [50], which can be utilized to unambiguously verify that the main contribution to the SHG signal comes from the bulk material rather than being a surface effect. On the practical side, the structure of the tensor allows nonlinear generation of a specific type of optical beams – vector beams – such as azimuthally or radially polarized light [53].

Periodic arrangements of nanoparticles, typically with a subwavelength period, are referred to as metasurfaces. Coupling between resonances of individual nanoparticles yields a more complicated spectral response beyond Mie theory. One of the advantageous consequences of such coupling is the emergence of dark modes of the metasurfaces; these modes do not couple to free-space, unless a defect is introduced that breaks the symmetry of the nanoparticle. The defect can couple dark mode to bright modes (i.e., modes that couple to free-space), causing a Fano-type interference [54] that shows up as a prominent narrow-band dip or peak in the transmittance or reflectance spectra [55,56]. Dark resonances support local fields that are larger by orders of magnitude compared to the fields of the incoming beam. A recent study of a GaAs-based Fano-resonant metasurface showed nontrivial spectral shaping of second-harmonic generation and multifold efficiency enhancement induced by high field localization and enhancement inside the broken-symmetry resonators [52].

The success of III–V-based nanostructures in achieving high SHG conversion efficiencies stems in part, from their high nonlinear susceptibility values, one of the

highest available (and typically non-phase matchable in bulk form). A downside is the relatively small values of the band gap energies, which translates into higher absorption coefficients for the harmonic generation radiation, impairing the conversion efficiency in certain spectral ranges [27]. Other material platforms have been utilized for efficient SHG at shorter wavelengths, with notable examples being perovskites (such as $BaTiO_3$ [57,35,33]), silicon carbide [32], and selenium [58]. Finally, a route to surpass the limitations of centrosymmetric materials is to create a nanocrystalline structure introducing interfaces where the symmetry is broken. For instance, in [34], SHG from a nanocrystalline silicon Mie nanoparticle was enhanced by two orders of magnitude with respect to an unstructured silicon film.

8.3.3.2 Third-harmonic generation

One of the most widespread and well-understood materials, silicon, has historically been the most popular source for all-dielectric nanophotonics structures, due to its abundance in nanotechnology and microelectronics. Being a centrosymmetric material, silicon exhibits little efficiency for second-order NLO effects. However, third-order nonlinearities are routinely measured through third-harmonic generation, two-photon absorption and other effects. Unsurprisingly, the first manifestations of nonlinearities enhanced by magnetic Mie-types resonances were found in silicon nanoparticles [22], where third-harmonic generation was found to be enhanced by two orders of magnitude with respect to a thick silicon wafer (Fig. 8.6A). The conversion efficiency was on the order of $\eta_{3\omega} \approx 10^{-7}$, on par with the best-performance plasmonic nanostructures. Over time, conversion efficiencies from the IR to visible and UV have been successfully optimized by choices of geometry, materials, polarization, spectral range and other parameters [59,22,26,25,60,31,61]. We give an account of THG conversion efficiency reports in Fig. 8.7.

Studies of THG from single nanoparticles can shed light on the role of different Mie resonances in their nonlinear response. As seen in Fig. 8.2, magnetic resonances are more likely to produce efficient THG than electric modes. This was experimentally and numerically verified in ref. [62], where single silicon nanodisks were excited by a tunable femtosecond laser source at either the electric or magnetic dipole resonances. Having a certain spatial distribution, these modes can be selectively excited by structured light beams, as revealed by enhanced THG [63]. Higher-order modes, such as anapole modes [64], have shown to further aid in efficient frequency conversion, as proved in refs. [31,61] (Fig. 8.6B). Here, amorphous germanium was used instead of silicon, as it has a larger refractive index of $n \approx 4$, and higher nonlinear susceptibility in the chosen spectral range. As a result, an enhancement of about 4 orders of magnitude was found with respect to an unstructured film (in addition to another three orders with respect to a silicon wafer) [31].

Optical resonators that are placed close to each other can provide additional degrees of freedom through optical coupling between the Mie modes of the individual resonators. If several nanoparticles are combined so that the distance between them is less or on the order of a wavelength, they are commonly referred to as oligomers [65]. Pairs of nanoparticles, or dimers, were shown to create hot spots of enhanced local fields [66] which were then used to tailor the THG in the far-field [23]. Changing

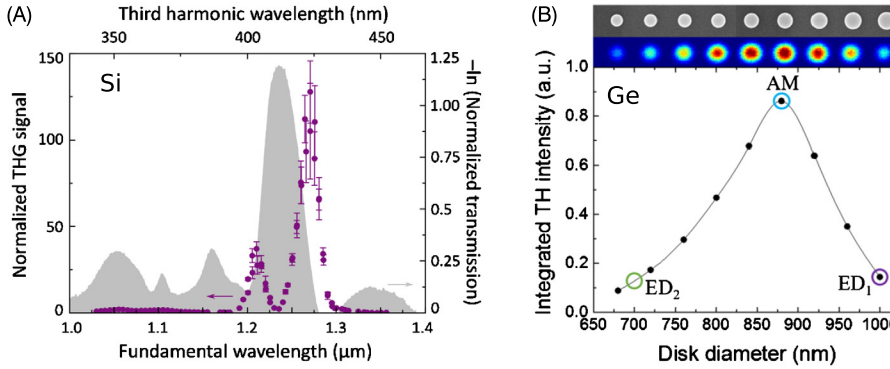

Figure 8.6 Third-harmonic generation from group IV semiconductor Mie-resonant nanostructures. (A) Third-harmonic output from a silicon metasurface normalized by THG intensity from an unstructured silicon wafer. Reproduced with permission from [22]. (B) Size-dependent third-harmonic generation from germanium nanodisks at a fixed wavelength reveals the maximum enhancement at the anapole mode (AM). Reproduced with permission from [31].

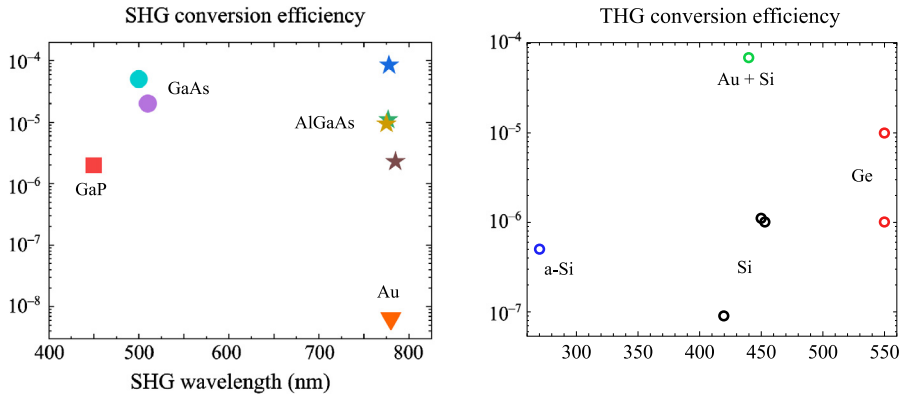

Figure 8.7 Experimentally measured conversion efficiencies of second- and third-harmonic generation processes in Mie-resonant nanostructures based on different materials. Left: GaP [28], GaAs [27,52], AlGaAs [53,30,50,51], and Au [71]. Right: a-Si [59,26,25], c-Si [22], a hybrid approach (Au + Si) [60], Ge [31,61].

the distance between the nanoparticles within oligomers modifies coupling between the individual nanoparticles' modes, which tunes their nonlinear response. In [37], oligomers consisting of three nanoparticles (trimers) excited at their magnetic dipole mode showed prominently different THG spectra for different sets of nanoparticle diameters and inter-particle spacing. Magnetic Fano resonances excited in subwavelength quadrumers provided additional enhancement of THG [25].

Quasi-infinite arrays of nanoparticles that have periods of less than a free-space wavelength – metasurfaces – can be used to further increase the nonlinear response when using high-quality factor (high-Q) collective modes. In [26], a metasurface with a Q-factor of up to 500 was used to enhance the THG by five orders of magnitude with

respect to a silicon film of the same thickness. A similar approach was used in [67] with a different structure that possesses dark modes with a small net dipole moment to enhance THG by a factor of 300 with respect to a bulk silicon substrate. Although high-Q metasurfaces represent a promising route to enhanced optical nonlinearities, both papers expressed concerns regarding wasting most of the bandwidth of the femtosecond pulse that is typically much wider than the bandwidth of the resonance. The time-bandwidth limit is a major obstacle to efficient interactions of femtosecond laser pulses with high-Q cavities, and the full advantage of the field enhancement within a high-Q cavity remains an open question.

Other functionalities of THG from Mie-resonant nanostructures are generation of UV light [59], manipulation of the nonlinear wavefront and directional nonlinear diffraction [68], enhanced nonlinearities by complementary structures [69], and possibilities in probing optical coupling of all-dielectric nanostructures to optical waveguides [70].

8.3.3.3 Other cases of frequency mixing

Second- and third-harmonic generation processes are enabled by the merging of two or three fundamental photons to a higher-energy photon, so that the overall energy is conserved: $\hbar\omega_n = n\hbar\omega$, where n is the process order. For a general frequency-mixing process, a nonlinear susceptibility can mix any number of photons having an arbitrary set of frequencies: $\sum_{i=1}^{N} \hbar\omega_i = \sum_{j=1}^{M} \hbar\omega_j$. First manifestations of four-wave mixing were provided in germanium nanodisks [72], where effective third-order susceptibilities as high as 2.8×10^{-16} m^2/V^2 were found. A more sophisticated technique utilized bi-color pump experiment, where 11 new frequencies were generated in III–V-based semiconductor metasurfaces [51]. It is important to note that the simultaneous mixing of such a vast amount of frequencies at comparable efficiencies is hard to observe in bulk materials, as the phase-matching conditions usually benefit one or few frequency conversion pathways while sacrificing the efficiency for others.

8.3.4 Self-action effects

In nonlinear materials, light beams can modify themselves without causing considerable conversion from one frequency to another. These effects, often referred to as self-action effects, give rise to a series of applications like power limiting, passive mode-locking, filament formation, solitons and others. Phenomenologically, these effects can be expressed by an intensity-dependent complex refractive index:

$$\tilde{n}(I) = \tilde{n}_0 + \tilde{n}_2 I, \tag{8.9}$$

where $\tilde{n}_0 = n_0 + i\kappa_0$ is the unperturbed complex refractive index, and $\tilde{n}_2 I = (n_2 + i\kappa_2)I$ is the part of the refractive index that is proportional to intensity. Since the refractive index depends on I, Mie resonances, which lead to field localization and enhancement, can substantially boost self-action in materials.

Self-action effects can be classified by the dominating term in $\tilde{n}_2 = n_2 + i\kappa_2$, either real or imaginary, and by its sign. Additionally, these effects can be categorized by the

physical nature behind $\tilde{n}_2$. Here, we will classify those effects that have been studied in Mie-resonant nanostructures.

8.3.4.1 Nonlinear absorption

If $n_2 = 0$ and $\kappa_2 > 0$, the effect is referred to as nonlinear absorption. More traditionally, it is expressed in terms of a nonlinear absorption coefficient $\alpha = \alpha_0 + \beta I$, which is interrelated with $\kappa = \alpha\lambda/4\pi$. The most common cause of nonzero nonlinear absorption is the two-photon absorption (TPA) process, which routinely occurs when a powerful IR laser pulse propagates through a semiconductor with the bandgap energy lying in the range of $2\hbar\omega > E_g > \hbar\omega$, where $\hbar\omega$ is the photon energy. Therefore, the simultaneous absorption of two photons can generate an electron–hole pair. Two-photon absorption has been extensively studied in all the commonly used semiconductors leading to applications in optical power limiters, mode-locking, etc.

In all-dielectric nanoantennas and metasurfaces, local fields can boost the nonlinear absorption cross-section, lowering the intensity requirements for optical limiting. For instance, a typical value for the TPA coefficient in silicon is on the order of $\beta = 1$ cm/GW [73]; for hydrogenated amorphous silicon it strongly depends on the lattice structure and hydrogen content, and was found to be on the order of $\beta = 10 - 100$ cm/GW [74]. Metasurfaces fabricated out of a thin amorphous silicon film enhance TPA by a factor of 80 with respect to an unpatterned film, resulting in a value of $\beta = 5600$ cm/GW [37]. Subsequent generation of free carriers can induce significant changes in the linear response of the nanoparticles, such as reflectance or scattering directionality [75].

8.3.4.2 Nonlinear refraction

When $n_2 \neq 0$ and $\kappa_2 = 0$, the situation is referred to as nonlinear refraction. There are numerous microscopic mechanisms that lead to an intensity-dependent refractive index; these can be separated into two major categories: parametric and non-parametric. The former, the optical Kerr effect, is defined by an instantaneous value of the electric field in the material and relies on the nonlinear coherent response of electrons in the material; this effect is usually fairly weak: $n_2 \approx 10^{-16} - 10^{-13}$ cm^2/W in common dielectrics and semiconductors. In most cases, this contribution to n is present only when light is within the material, as electron decoherence times are on the femtosecond scale, which is shorter than the vast majority of the pulsed light sources. Since the Kerr effect magnitude is weak, parametric nonlinear refraction in nanostructures has been usually considered elusive; however, novel materials such chalcogenide glasses look promising in this context [76].

In contrast, the non-parametric additions to n are not connected to the nonlinearity of the electron response, and are not due to the presence of light *per se* but rather due to the changes in the material parameters such as temperature or the concentration of free charge carriers. Light can heat materials causing thermally induced changes in $n = n_0 + Tdn/dT = n_0 + I(dT/dI)(dn/dT)$. The large values of refractive index modulation come at the expense of speed: recovery takes microseconds or even seconds (although faster relaxation times can occur at the nanoscale).

A much faster process of index modulation is photogeneration of free carriers, created through either single- or multi-photon absorption processes in semiconductors. Here, $n = n_0 + \Delta n_{FC}$, where Δn_{FC} is the refractive index addition, usually negative, caused by the photogenerated electron–hole pairs. We will discuss this type of nonlinearity further in section 8.4.2.

8.3.5 High-order effects

Eq. (8.3) is a Taylor series with E/E_{at} as the expansion parameter, where E is the incident field strength and $E_{at} \approx 5 \cdot 10^{11}$ V/m. Under the condition of $E \ll E_{at}$, nonlinear polarization is much smaller than the linear one and the regime is called perturbative. The closer the E is to E_{at}, the more inaccurately the series describes the real polarization of materials, as the high-order terms become comparable to each other. In GaAs, for instance, one can estimate the critical intensity at which $P^{(2)} \approx P^{(3)}$, or, conversely, $E_{crit} \approx \chi^{(2)}/\chi^{(3)} \approx 10^9$ V/m, which corresponds to intensities of approximately 1 TW/cm^2. This so-called non-perturbative regime has become accessible through both the advent of femtosecond laser sources, which can easily reach such intensities, and resonant nanostructures [77], which can funnel light to hot spots of much higher field intensity than the incident light.

The most straightforward manifestation of non-perturbative nonlinearities is the process of high-harmonic generation (HHG). In solids, photogenerated free electrons move in highly non-parabolic potentials due to large spatial displacements, generating optical harmonics in the extreme UV [78]. The intensity requirements for this process are high, and one of the approaches to significantly reducing them is to use localized resonances. Semiconductor metasurfaces with Mie-type resonances have been successfully used to observe even harmonics up to the fourth in noncentrosymmetric materials [51] and odd harmonics up to the 11th in silicon-based metasurfaces [79]. The ninth harmonic from the metasurface can be detected at intensities as low as 50 GW/cm^2 with the signal two orders of magnitude above the noise level, whereas any detectable ninth harmonic from an unpatterned film of the same thickness shows up only at 200 GW/cm^2 [79].

One of the most straightforward results of Eq. (8.3) is that, if pumped by a narrowband laser centered at frequency ω, the resulting harmonics will have spectra centered at $n\omega$, where n is the order of the nonlinear process. On the other hand, this rule may fail in dynamically evolving systems, such as rapidly generated plasmas in gases and semiconductors [80]. In these systems, generation of free carriers leads to blue shifting of the emitted fundamental and harmonic generation, a process sometimes dubbed "photon acceleration" [81]. However, typical intensities of 10^{15} W/cm^2 are needed to observe considerable blue-shifts of the emitted photons. At much lower intensities of up to 30 GW/cm^2, photon acceleration has been recently revealed in semiconductor metasurfaces by observing the spectrum of the THG radiation blue-shift as the pump intensity is increased [82]. In this experiment, the generated photons had a variable carrier frequency from 3ω to 3.1ω, tuned by the intensity of the mid-infrared pump, thus expanding the scope of frequency conversion beyond integer harmonics.

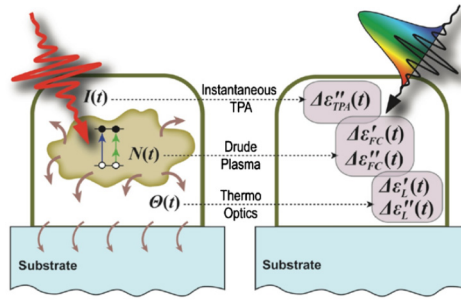

Figure 8.8 Ultrafast processes in semiconductor nanostructures. Reproduced with permission after [38].

8.4 Ultrafast phenomena in Mie-resonant nanostructures

By convention, ultrafast phenomena are those with relaxation time of approximately 1 ps and shorter [83], allowing characteristic modulation frequencies of more than 1 THz. Since few electric-current-based devices can provide bandwidths above several hundreds of GHz, many people consider the all-optical approach to be a major candidate for ultrafast signal processing.

Ultrafast processes in materials are routinely investigated using pump–probe spectroscopy, or time-resolved spectroscopy. A powerful ultrashort laser pulse ("pump") causes modifications to the materials under study that are then probed by a weaker pulse ("probe") in the form of transmittance, reflectance, scattering, polarization or frequency conversion. The response of the probe is monitored as a function of the time delay between the pulses, reconstructing the relaxation process of the material. The probe and the pump can have different polarizations, frequencies, and temporal profiles, so as to reveal different aspects of the underlying processes (Fig. 8.8).

Semiconductors are the most popular materials for all-dielectric Mie-resonant nanostructures. The most common semiconductors – silicon, germanium, gallium arsenide and others – have been extensively studied using pump–probe spectroscopy. A simplified timeline of the microscopic processes following a femtosecond pulse impinging on a surface of a bulk semiconductor is as follows [84]:

- $\tau < 200$ fs: Free carriers (FCs) are generated through single- or multi-photon absorption. At this point in time, the electromagnetic field is typically still within the material, thus opened to coherent frequency-mixing processes. FCs lose coherence via carrier-carrier scattering events. The energy distribution is non-Boltzmann, i.e., the electron gas has not yet thermalized.
- $\tau < 2$ ps: Electrons and holes have thermalized to Boltzmann-type energy distributions. The electron-lattice energy exchange is under way through electron–phonon scattering. Light is no longer present in the material.
- $\tau < 100$ ps: Electrons and holes have lost their energy to phonons and recombined. Lattice is sinking its excess energy to the environment. The end time of this process is highly dependent on many parameters, including substrate material.

In every step of this process, the transient value of the complex dielectric permittivity of the material $\tilde{\varepsilon}(t)$ differs from its equilibrium value $\tilde{\varepsilon}_0$: $\tilde{\varepsilon}(t) = \tilde{\varepsilon}_0 + \Delta\tilde{\varepsilon}(t)$. There are three main contributions to $\Delta\tilde{\varepsilon}$: the instantaneous one (as discussed in Section 8.3.4.2), the one induced by the presence of the free carriers $\Delta\tilde{\varepsilon}_{\mathrm{FC}}$ and the one induced by lattice heating, or the presence of phonons $\Delta\tilde{\varepsilon}_L$. The free-carrier contribution is the one that is often utilized in all-optical switches [85]. However, in bulk semiconductors, recombination of free carriers is a slow process that does not allow for ultrafast relaxation times.

Fortunately, in nanostructures and under high intensity laser illumination, the recombination processes can happen much faster, enabling novel devices that could operate at ultrafast modulation frequencies. The general (simplified) recombination rate equation for FC density $N(t)$ is [86]:

$$\frac{dN}{dt} = -AN - BN^2 - CN^3, \tag{8.10}$$

where A, B, and C are the monomolecular, bimolecular and Auger recombination rates. These coefficients are specific to a given semiconductor. For a typical example, in bulk GaAs, $A < 5 \times 10^7$ s^{-1}, $B = (1.7 \pm 0.2) \times 10^{-10}$ cm^3/s, and $C = (7 \pm 14) \times 10^{30}$ cm^6/s [86]. At low pump intensities, Eq. (8.10) leads to N being less than 10^{18} cm^{-3}; the first term in Eq. (8.10) dominates over the second and the third ones, giving a relaxation time of 200 ns. This figure can be improved by either increasing the pump intensity leading to a higher FC density, or decreasing the value of A. The latter can be achieved by introducing impurities (a good example being low-temperature-grown GaAs) or by increasing the surface area by nanostructuring [87]. Both approaches have been utilized in semiconductor metasurfaces, as shown below.

8.4.1 Instantaneous all-optical modulation

The only instantaneous mechanisms of all-optical modulation implemented so far in semiconductor metasurfaces are two-photon absorption (TPA) and frequency mixing. TPA manifests itself as a sharp dip at near-zero delay on time-resolved transmittance or reflectance traces [37,26,38], with a duration of the dip limited to the duration of the optical pulses used in the experiment. For typical TPA dips in pump–probe traces for metasurfaces, see Fig. 8.9C. Frequency mixing, as discussed in previous sections, can be cross-modulated by two separate beams, allowing all-optical modulation of the resulting signal [51]; see Fig. 8.9D. Instantaneous phenomena, in sharp contrast with the free-carrier-related contributions, allow for potential switching rates at frequencies of more than 10 THz, paving the way to ultrafast logic gates using photonics.

8.4.2 Free-carrier effects

Optical response of a semiconductor that contains free carriers, such as electrons and/or holes, is frequently dominated by the Drude dispersion of the dielectric per-

mittivity:

$$\varepsilon(\omega) = \varepsilon_\infty - \frac{\omega_p^2}{\omega^2 + i\gamma\omega}, \tag{8.11}$$

where $\omega_p = \sqrt{Ne^2/\varepsilon_0 m^*}$ is the plasma frequency, N is the free-carrier concentration, e is the elementary charge, m^* is the effective free-carrier mass, and γ is the damping constant. This approximation holds for most experimental cases, especially when the probe beam's photon energy is below the band gap, and if the free-carrier concentration is sufficiently low. Free carriers have experimentally changed the refractive index by up to $\Delta n/n \approx -0.04$ in metasurfaces [88], which, with an appropriate Q-factor of the resonance, can shift its central frequency by about its full width at half maximum (causing considerable changes in reflectance of up to 0.35). The presence of free carriers in Mie-resonant semiconductor nanoparticles not only changes the back- or forward-scattering of light but tailors the scattering pattern in general, as shown by several theoretical efforts [89–91].

The rate of relaxation to the initial state strongly depends on the material used as the constituent material for a metasurface. Crystalline materials with an indirect band gap, such as silicon, are poor candidates for ultrafast metasurfaces, as relaxation times in these materials can be as long as hundreds of picoseconds [92]. This can be mitigated by introducing higher-order terms of the rate Eq. (8.10) through hard pumping of the metasurfaces. In Ref. [90], silicon nanoparticles were pumped at high fluences of around 40 mJ/cm^2 so as to achieve large estimated FC density of about 5×10^{20} cm^{-3}. This led to dominance of the Auger recombination process, making it as fast as 2.5 ps; see Fig. 8.9A for a typical pump–probe trace.

Another approach to shortening the lifetime of FCs in a semiconductor is to increase the probability of monomolecular recombination through inhomogeneities of the crystal structure or non-radiative centers. Fortunately, metasurfaces naturally possess an increased relative surface area due to nanostructuring, which increases the likelihood of surface recombination. This effect was shown to dominate the relaxation in GaAs-based metasurfaces, leading to relaxation of the magnetic dipolar Mie-mode back to its initial state in only 6 ps and $1/e$ relaxation time of 2.5 ps [88]; see Fig. 8.9B.

In general and beyond the Drude approximation, the refractive index change relies on three main components [93]: the Drude term, the band filling effect and the band shrinkage effect. The resulting index modulation is given by

$$\Delta n = \Delta n_{\mathrm{D}} + \Delta n_{\mathrm{BF}} + \Delta n_{\mathrm{BS}}. \tag{8.12}$$

The extra terms may become important in some experimental cases [88]. As an example, the band filling effect on the refractive index is defined by the decline of the interband transitions due to occupation of the electron and hole states in the conduction and valence bands, respectively. In the parabolic band approximation, the interband absorption is given by the following expression:

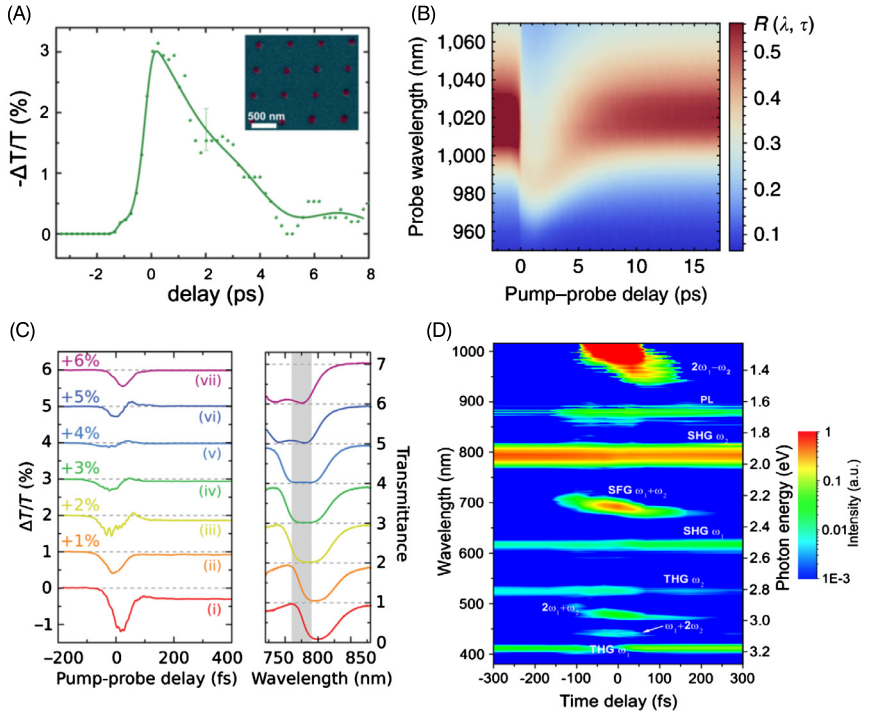

Figure 8.9 Routes to ultrafast all-optical modulation in semiconductor metasurfaces. (A) At high FC concentrations, bimolecular and Auger terms lead to faster recombination, enabling relaxation times of 2.5 ps in a-Si. Reprinted with permission from [90]. (B) Surface recombination in direct-gap semiconductors (GaAs) can provide rapid all-optical tuning of the resonance and relaxation times of 2.5 ps. Reprinted with permission from [88]. (C) Overcoming FC contributions by judicious choice of the pump wavelength versus the resonance wavelength for coherent all-optical modulation. Reprinted with permission from [37]. (D) Utilizing parametric frequency-mixing processes facilitates ultrafast, subpicosecond all-optical response. Reprinted with permission from [51].

$$\alpha(E) = \begin{cases} 0, & \text{if } E \le E_g, \\ \frac{C_{hh}}{E}\sqrt{E - E_g} + \frac{C_{lh}}{E}\sqrt{E - E_g}, & \text{if } E > E_g. \end{cases} \tag{8.13}$$

For instance, in GaAs, $C_{hh} = 3.1 \cdot 10^6$ cm^{-1}eV$^{1/2}$ and $C_{lh} = 1.6 \cdot 10^6$ cm^{-1}eV$^{1/2}$, and $E_g = 1.42$ eV is the band gap width of GaAs at room temperature. Absorption of GaAs saturates as the bands get filled, as given by

$$\begin{aligned} \Delta\alpha = &\frac{C_{hh}}{E}\sqrt{E - E_g}[f_v(E_{ah}) - f_c(E_{bh}) - 1] \\ &+ \frac{C_{lh}}{E}\sqrt{E - E_g}[f_v(E_{al}) - f_c(E_{bl}) - 1], \end{aligned} \tag{8.14}$$

where $f_c(E_{bh,bl})$ and $f_v(E_{ah,al})$ are the Fermi–Dirac distributions in for electrons and holes, respectively. The band shrinkage effect is phenomenologically introduced as E_g being directly dependent on the carrier concentration: $\Delta E_g \propto -N^{1/3}$, which in

turn, affects Eq. (8.13). The refractive index addition by both band filling and band shrinkage are then calculated through Kramers–Kronig relations from Eq. (8.13). The full derivation of these contributions in some of III–Vs is given in [93]. In metasurfaces operating at photon energies close to the band gap of GaAs, ≈ 1.24 eV, the band filling contribution was shown to be equally important in all-optical tuning of the Mie-resonance as the Drude term [88].

8.5 Conclusions and outlook

Although nonlinear and ultrafast properties of Mie-resonant nanostructures have been extensively studied for more than 5 years, it is still a developing field with many unknowns. Below, we attempt to outline a roadmap of this exciting area of nanophotonics.

8.5.1 Beyond the visible and near-IR

Studies of nonlinear all-dielectric metamaterials have been traditionally limited to the near-IR and visible spectral regions. On the other hand, many applications, such as molecular fingerprinting, night vision, and others, require efficient nonlinear materials in other spectral ranges. Mid-infrared radiation, or radiation with wavelengths of $\lambda = 3-12$ μm, is an important spectral range, for it carries information about chemical composition of materials and contains most of the thermal radiation emitted at room temperature and higher. Relevant to nonlinear materials, the following features of the mid-IR are of particular interest:

- The most common semiconductor materials, such as Si, GaAs, Ge and many others, are transparent in the mid-IR, granted by the low energies of optical phonons in these materials.
- Nonlinear absorption is lower than that seen in the near-IR, since it requires more photons to induce an interband transition of an electron to the conduction band.
- Generation of free carriers has a larger effect on the dielectric permittivity of semiconductors. The Drude term, which dominates the permittivity of semiconductors in the mid-IR, scales as $\propto \lambda^2$, lowering the power requirements to all-optical switching.
- Optical properties of semiconductors, such as their band gap and resonant polarizabilities, can be manipulated by growth of heterostructures with inter-subband transitions, which has already been implemented for plasmonic nanostructures [94,95].

For these and other reasons, the mid-IR spectral range has been hailed as one of the possible directions for integrated photonics [96,97]. We predict an elevated interest of the community to this region in the coming years. For similar reasons, the THz band has also been attractive for ultrafast and nonlinear response of semiconductor-based metamaterials.

8.5.2 Emerging materials

The current roster of materials for nonlinear Mie-resonant nanoparticles and metasurfaces has mainly contained silicon, germanium, and $Al_xGa_{1-x}As$, with few exceptions. On the other hand, a variety of high-index materials for Mie-resonant photonics has been used to date, many of which are promising nonlinear materials too. We expect more exciting results in the nearest future from the following platforms: traditional nonlinear crystals such as $LiNbO_3$ [23], large bandgap materials such as GaN, GaP and others [28], diamond [98], and nanostructures with tailored intersubband transitions [94,95], as well as various phase-change materials. From the ultrafast perspective, of interest are materials with defects – such as low-temperature-grown GaAs and amorphous Ge – and materials with low effective FC masses, such as narrow-gap semiconductors like InSb, engineered superlattices [99], as well as graphene and other 2D materials.

8.5.3 Exotic nonlinearities

The richness of NLO lies beyond generation of harmonics, nonlinear absorption and all-optical modulation. Many rarer, yet no less intriguing NLO effects are yet to be observed in Mie-resonant systems. These effects include, to name a few: electric-field-induced second-harmonic generation in centrosymmetric materials, tunneling ionization and ponderomotive effects, Franz–Keldysh effect, ultrafast magnetism [100], optical rectification and generation of THz radiation, as well as effects emerging through time-varying refractive index. With the expansion of material platforms and spectral range, we envision exciting opportunities in nonlinear all-dielectric and semiconductor metamaterials.

References

[1] P.A. Franken, A.E. Hill, C.W. Peters, G. Weinreich, Generation of optical harmonics, Phys. Rev. Lett. 7 (1961) 118.
[2] M.W. Klein, C. Enkrich, M. Wegener, S. Linden, Second-harmonic generation from magnetic metamaterials, Science 313 (2006) 502.
[3] M. Ren, B. Jia, J.Y. Ou, E. Plum, J. Zhang, K.F. MacDonald, A.E. Nikolaenko, J. Xu, M. Gu, N.I. Zheludev, Nanostructured plasmonic medium for terahertz bandwidth all-optical switching, Adv. Mater. 23 (2011) 5540.
[4] M. Kauranen, A.V. Zayats, Nonlinear plasmonics, Nat. Photonics 6 (2012) 737.
[5] S. Jahani, Z. Jacob, All-dielectric metamaterials, Nat. Nanotechnol. 11 (2016) 23.
[6] A.I. Kuznetsov, A.E. Miroshnichenko, M.L. Brongersma, Y.S. Kivshar, B. Lukyanchuk, Optically resonant dielectric nanostructures, Science 354 (2016) aag2472.
[7] P. Kapitanova, V. Ternovski, A. Miroshnichenko, N. Pavlov, P. Belov, Y. Kivshar, M. Tribelsky, Giant field enhancement in high-index dielectric subwavelength particles, Sci. Rep. 7 (2017) 731.
[8] R.W. Boyd, Nonlinear Optics, 3rd ed., Academic Press, 2008.
[9] Y.R. Shen, The Principles of Nonlinear Optics, Wiley–Interscience, New York, 1984.

[10] H.J. Simon, D.E. Mitchell, J.G. Watson, Optical second-harmonic generation with surface plasmons in silver films, Phys. Rev. Lett. 33 (1974) 1531.
[11] C.K. Chen, A.R.B. De Castro, Y.R. Shen, Surface-enhanced second-harmonic generation, Phys. Rev. Lett. 46 (1981) 145.
[12] L. Tsang, D. Ahn, S.L. Chuang, Electric field control of optical second-harmonic generation in a quantum well, Appl. Phys. Lett. 52 (1988) 697.
[13] P. Boucaud, F.H. Julien, D.D. Yang, J. Lourtioz, E. Rosencher, P. Bois, J. Nagle, Detailed analysis of second-harmonic generation near 10.6 μm in GaAs/AlGaAs asymmetric quantum wells, Appl. Phys. Lett. 57 (1990) 215.
[14] V. Berger, Nonlinear photonic crystals, Phys. Rev. Lett. 81 (1998) 4136.
[15] M. Soljac, J.D. Joannopoulos, Enhancement of nonlinear effects using photonic crystals, Nat. Mater. 3 (2004) 211.
[16] B. Corcoran, C. Monat, C. Grillet, D.J. Moss, B.J. Eggleton, T.P. White, L. O'Faolain, T.F. Krauss, Green light emission in silicon through slow-light enhanced third-harmonic generation in photonic-crystal waveguides, Nat. Photonics 3 (2009) 206.
[17] J. Leuthold, C. Koos, W. Freude, Nonlinear silicon photonics, Nat. Photonics 4 (2010) 535.
[18] A.I. Kuznetsov, A.E. Miroshnichenko, Y.H. Fu, J. Zhang, B. Luk'yanchuk, Magnetic light, Sci. Rep. 2 (2012) 492.
[19] A.B. Evlyukhin, S.M. Novikov, U. Zywietz, R.L. Eriksen, C. Reinhardt, S.I. Bozhevolnyi, B.N. Chichkov, Demonstration of magnetic dipole resonances of dielectric nanospheres in the visible region, Nano Lett. 12 (2012) 3749.
[20] J.C. Ginn, I. Brener, D.W. Peters, J.R. Wendt, J.O. Stevens, P.F. Hines, L.I. Basilio, L.K. Warne, J.F. Ihlefeld, P.G. Clem, M.B. Sinclair, Realizing optical magnetism from dielectric metamaterials, Phys. Rev. Lett. 108 (2012) 097402.
[21] C.F. Bohren, D.R. Huffmman, Absorption and Scattering of Light by Small Particles, Wiley, New York, 2004.
[22] M.R. Shcherbakov, D.N. Neshev, B. Hopkins, A.S. Shorokhov, I. Staude, E.V. Melik-gaykazyan, M. Decker, A.A. Ezhov, A.E. Miroshnichenko, I. Brener, A.A. Fedyanin, Y.S. Kivshar, Enhanced third-harmonic generation in silicon nanoparticles driven by magnetic response, Nano Lett. 14 (2014) 6488.
[23] L. Wang, S. Kruk, L. Xu, M. Rahmani, D. Smirnova, A. Solntsev, I. Kravchenko, D. Neshev, Y. Kivshar, Shaping the third-harmonic radiation from silicon nanodimers, Nanoscale 9 (2017) 2201.
[24] M.R. Shcherbakov, A.S. Shorokhov, D.N. Neshev, B. Hopkins, I. Staude, E.V. Melik-Gaykazyan, A.A. Ezhov, A.E. Miroshnichenko, I. Brener, A.A. Fedyanin, Y.S. Kivshar, Nonlinear interference and tailorable third-harmonic generation from dielectric oligomers, ACS Photonics 2 (2015) 578.
[25] A.S. Shorokhov, E.V. Melik-Gaykazyan, D.A. Smirnova, B. Hopkins, K.E. Chong, D.Y. Choi, M.R. Shcherbakov, A.E. Miroshnichenko, D.N. Neshev, A.A. Fedyanin, Y.S. Kivshar, Multifold enhancement of third-harmonic generation in dielectric nanoparticles driven by magnetic Fano resonances, Nano Lett. 16 (2016) 4857.
[26] Y. Yang, W. Wang, A. Boulesbaa, I.I. Kravchenko, D.P. Briggs, A. Puretzky, D. Geohegan, J. Valentine, Nonlinear Fano-resonant dielectric metasurfaces, Nano Lett. 15 (2015) 7388.
[27] S. Liu, M.B. Sinclair, S. Saravi, G.A. Keeler, Y. Yang, J. Reno, G.M. Peake, F. Setzpfandt, I. Staude, T. Pertsch, I. Brener, Resonantly enhanced second-harmonic generation using III–V semiconductor all-dielectric metasurfaces, Nano Lett. 16 (2016) 5426.

[28] J. Cambiasso, G. Grinblat, Y. Li, A. Rakovich, E. Cortés, S.A. Maier, Bridging the gap between dielectric nanophotonics and the visible regime with effectively lossless gallium phosphide antennas, Nano Lett. 17 (2017) 1219.
[29] L. Carletti, A. Locatelli, O. Stepanenko, G. Leo, C. De Angelis, Enhanced second-harmonic generation from magnetic resonance in AlGaAs nanoantennas, Opt. Express 23 (2015) 26544.
[30] V.F. Gili, L. Carletti, A. Locatelli, D. Rocco, M. Finazzi, L. Ghirardini, I. Favero, C. Gomez, A. Lemaître, M. Celebrano, C. De Angelis, G. Leo, Monolithic AlGaAs second-harmonic nanoantennas, Opt. Express 24 (2016) 15965.
[31] G. Grinblat, Y. Li, M.P. Nielsen, R.F. Oulton, S.A. Maier, Enhanced third harmonic generation in single germanium nanodisks excited at the anapole mode, Nano Lett. 16 (2016) 4635.
[32] C.R. Ma, J.H. Yan, Y.M. Wei, G.W. Yang, Second harmonic generation from an individual amorphous selenium nanosphere, Nanotechnology 27 (2016) 425206.
[33] C. Ma, J. Yan, Y. Wei, P. Liu, G. Yang, Enhanced second harmonic generation in individual barium titanate nanoparticles driven by Mie resonances, J. Mater. Chem. C 5 (2017) 4810.
[34] S.V. Makarov, M.I. Petrov, U. Zywietz, V. Milichko, D. Zuev, N. Lopanitsyna, A. Kuksin, I. Mukhin, G. Zograf, E. Ubyivovk, D.A. Smirnova, S. Starikov, B.N. Chichkov, Y.S. Kivshar, Efficient second-harmonic generation in nanocrystalline silicon nanoparticles, Nano Lett. 17 (2017) 3047.
[35] F. Timpu, A. Sergeyev, N.R. Hendricks, R. Grange, Second-harmonic enhancement with Mie resonances in perovskite nanoparticles, ACS Photonics 4 (2017) 76.
[36] I. Staude, A.E. Miroshnichenko, M. Decker, N.T. Fofang, S. Liu, E. Gonzales, J. Dominguez, T.S. Luk, D.N. Neshev, I. Brener, Y. Kivshar, Tailoring directional scattering through magnetic and electric resonances in subwavelength silicon nanodisks, ACS Nano 7 (2013) 7824.
[37] M.R. Shcherbakov, P.P. Vabishchevich, A.S. Shorokhov, K.E. Chong, D.Y. Choi, I. Staude, A.E. Miroshnichenko, D.N. Neshev, A.A. Fedyanin, Y.S. Kivshar, Ultrafast all-optical switching with magnetic resonances in nonlinear dielectric nanostructures, Nano Lett. 15 (2015) 6985.
[38] G. Della Valle, B. Hopkins, L. Ganzer, T. Stoll, M. Rahmani, S. Longhi, Y.S. Kivshar, C. De Angelis, D.N. Neshev, G. Cerullo, Nonlinear anisotropic dielectric metasurfaces for ultrafast nanophotonics, ACS Photonics 4 (2017) 2129.
[39] L. Xu, M. Rahmani, K. Zangeneh Kamali, A. Lamprianidis, L. Ghirardini, J. Sautter, R. Camacho-Morales, H. Chen, M. Parry, I. Staude, G. Zhang, D. Neshev, A.E. Miroshnichenko, Boosting third-harmonic generation by a mirror-enhanced anapole resonator, Light: Sci. Appl. 7 (2018).
[40] G. Grinblat, R. Berte, M.P.P. Nielsen, Y. Li, R.F. Oulton, S.A. Maier, Sub-20 fs all-optical switching in a single Au-Clad Si nanodisk, Nano Lett. 18 (2018) 7896.
[41] S. Liu, G.A. Keeler, J.L. Reno, M.B. Sinclair, I. Brener, III–V semiconductor nanoresonators – a new strategy for passive, active, and nonlinear all-dielectric metamaterials, Adv. Opt. Mater. 4 (2016) 1457.
[42] T.V. Dolgova, A.I. Maidykovski, M.G. Martemyanov, A.A. Fedyanin, O.A. Aktsipetrov, G. Marowsky, V.A. Yakovlev, G. Mattei, Giant microcavity enhancement of second-harmonic generation in all-silicon photonic crystals, Appl. Phys. Lett. 81 (2002) 2725.
[43] M.G. Martemyanov, E.M. Kim, T.V. Dolgova, A.A. Fedyanin, O.A. Aktsipetrov, G. Marowsky, Third-harmonic generation in silicon photonic crystals and microcavities, Phys. Rev. B 70 (2004) 073311.

[44] S. Liu, G.A. Keeler, J. Reno, Y. Yang, M.B. Sinclair, I. Brener, Efficient second harmonic generation from GaAs all-dielectric metasurfaces, CLEO:QELS_Fundam. Sci. 1 (2016) 2.

[45] S.S. Kruk, R. Camacho-Morales, L. Xu, M. Rahmani, D.A. Smirnova, L. Wang, H.H. Tan, C. Jagadish, D.N. Neshev, Y.S. Kivshar, Nonlinear optical magnetism revealed by second-harmonic generation in nanoantennas, Nano Lett. 17 (2017) 3914.

[46] F.J. Löchner, A.N. Fedotova, S. Liu, G.A. Keeler, G.M. Peake, S. Saravi, M.R. Shcherbakov, S. Burger, A.A. Fedyanin, I. Brener, T. Pertsch, F. Setzpfandt, I. Staude, Polarization-dependent second harmonic diffraction from resonant GaAs metasurfaces, ACS Photonics 5 (2018) 1786.

[47] M. Sheik-Bahae, A.A. Said, T.H. Wei, D.J. Hagan, E.W.V. Stryland, Sensitive measurements of optical nonlinearities using a single beam, IEEE J. Quantum Electron. 26 (1990) 760.

[48] L. Carletti, D. Rocco, A. Locatelli, C. De Angelis, V.F. Gili, M. Ravaro, I. Favero, G. Leo, M. Finazzi, L. Ghirardini, M. Celebrano, G. Marino, A.V. Zayats, Controlling second-harmonic generation at the nanoscale with monolithic AlGaAs-on-AlOx antennas, Nanotechnology 28 (2017) 114005.

[49] R. Sanatinia, M. Swillo, S. Anand, Surface second-harmonic generation from vertical GaP nanopillars, Nano Lett. 12 (2012) 820.

[50] L. Ghirardini, L. Carletti, V. Gili, G. Pellegrini, L. Duò, M. Finazzi, D. Rocco, A. Locatelli, C. De Angelis, I. Favero, M. Ravaro, G. Leo, A. Lemaître, M. Celebrano, Polarization properties of second-harmonic generation in AlGaAs optical nanoantennas, Opt. Lett. 42 (2017) 559.

[51] S. Liu, P.P. Vabishchevich, A. Vaskin, J.L. Reno, G.A. Keeler, M.B. Sinclair, I. Staude, I. Brener, An all-dielectric metasurface as a broadband optical frequency mixer, Nat. Commun. 9 (2018) 2507.

[52] P.P. Vabishchevich, S. Liu, M.B. Sinclair, G.A. Keeler, G.M. Peake, I. Brener, Enhanced second-harmonic generation using broken symmetry III–V semiconductor Fano metasurfaces, ACS Photonics 5 (2018) 1685.

[53] R. Camacho-Morales, M. Rahmani, S. Kruk, L. Wang, L. Xu, D.A. Smirnova, A. Solntsev, A.E. Miroshnichenko, H.H. Tan, F. Karouta, S. Naureen, K. Vora, L. Carletti, C. de Angelis, C. Jagadish, Y.S. Kivshar, D.N. Neshev, Nonlinear generation of vector beams from AlGaAs nanoantennas, Nano Lett. 16 (2016) 7191.

[54] M.F. Limonov, M.V. Rybin, A.N. Poddubny, Y.S. Kivshar, Fano resonances in photonics, Nat. Photonics 11 (2017) 543.

[55] Y. Yang, I.I. Kravchenko, D.P. Briggs, J. Valentine, All-dielectric metasurface analogue of electromagnetically induced transparency, Nat. Commun. 5 (2014) 5753.

[56] S. Campione, S. Liu, L.I. Basilio, L.K. Warne, W.L. Langston, T.S. Luk, J.R. Wendt, J.L. Reno, G.A. Keeler, I. Brener, M.B. Sinclair, Broken symmetry dielectric resonators for high quality factor Fano metasurfaces, ACS Photonics 3 (2016) 2362.

[57] F. Timpu, N.R. Hendricks, M. Petrov, S. Ni, C. Renaut, H. Wolf, L. Isa, Y. Kivshar, R. Grange, Enhanced second-harmonic generation from sequential capillarity-assisted particle assembly of hybrid nanodimers, Nano Lett. 17 (2017) 5381.

[58] C.R. Ma, J.H. Yan, P. Liu, Y.M. Wei, G.W. Yang, Second harmonic generation from an individual all-dielectric nanoparticle: resonance enhancement versus particle geometry, J. Mater. Chem. C 4 (2016) 6063.

[59] S.V. Makarov, A.N. Tsypkin, T.A. Voytova, V.A. Milichko, I.S. Mukhin, A.V. Yulin, S.E. Putilin, M.A. Baranov, A.E. Krasnok, I.A. Morozov, P.A. Belov, Self-adjusted all-

dielectric metasurfaces for deep ultraviolet femtosecond pulse generation, Nanoscale 8 (2016) 17809.

[60] T. Shibanuma, G. Grinblat, P. Albella, S.A. Maier, Efficient third harmonic generation from metal-dielectric hybrid nanoantennas, Nano Lett. 17 (2017) 2647.

[61] G. Grinblat, Y. Li, M.P. Nielsen, R.F. Oulton, S.A. Maier, Efficient third harmonic generation and nonlinear subwavelength imaging at a higher-order anapole mode in a single germanium nanodisk, ACS Nano 11 (2017) 953.

[62] E.V. Melik-Gaykazyan, M.R. Shcherbakov, A.S. Shorokhov, I. Staude, I. Brener, D.N. Neshev, Y.S. Kivshar, A.A. Fedyanin, Third-harmonic generation from Mie-type resonances of isolated all-dielectric nanoparticles, Philos. Trans. R. Soc. A 375 (2017) 20160281.

[63] E.V. Melik-Gaykazyan, S.S. Kruk, R. Camacho-Morales, L. Xu, M. Rahmani, K. Zangeneh Kamali, A. Lamprianidis, A.E. Miroshnichenko, A.A. Fedyanin, D.N. Neshev, Y.S. Kivshar, Selective third-harmonic generation by structured light in Mie-resonant nanoparticles, ACS Photonics 5 (2018) 728.

[64] A.E. Miroshnichenko, A.B. Evlyukhin, Y.F. Yu, R.M. Bakker, A. Chipouline, A.I. Kuznetsov, B. Luk'yanchuk, B.N. Chichkov, Y.S. Kivshar, Nonradiating anapole modes in dielectric nanoparticles, Nat. Commun. 6 (2015) 8069.

[65] B. Hopkins, A.N. Poddubny, A.E. Miroshnichenko, Y.S. Kivshar, Revisiting the physics of Fano resonances for nanoparticle oligomers, Phys. Rev. A 88 (2013) 053819.

[66] R.M. Bakker, D. Permyakov, Y.F. Yu, D. Markovich, R. Paniagua-Domínguez, L. Gonzaga, A. Samusev, Y. Kivshar, B. Lukyanchuk, A.I. Kuznetsov, Magnetic and electric hotspots with silicon nanodimers, Nano Lett. 15 (2015) 2137.

[67] W. Tong, C. Gong, X. Liu, S. Yuan, Q. Huang, J. Xia, Y. Wang, Enhanced third harmonic generation in a silicon metasurface using trapped mode, Opt. Express 24 (2016) 19661.

[68] L. Wang, S.S. Kruk, K.L. Koshelev, I.I. Kravchenko, B. Luther-Davies, Y.S. Kivshar, Nonlinear wavefront control with all-dielectric metasurfaces, Nano Lett. 18 (2018) 3978.

[69] S. Chen, M. Rahmani, K.F. Li, A. Miroshnichenko, T. Zentgraf, G. Li, D. Neshev, S. Zhang, Third harmonic generation enhanced by multipolar interference in complementary silicon metasurfaces, ACS Photonics 5 (2018) 1671.

[70] K.I. Okhlopkov, A.A. Ezhov, P. Shafirin, N.A. Orlikovsky, M.R. Shcherbakov, A.A. Fedyanin, Optical coupling between resonant dielectric nanoparticles and dielectric waveguides probed by third harmonic generation microscopy, ACS Photonics 6 (2019) 189.

[71] M. Celebrano, X. Wu, M. Baselli, S. Großmann, P. Biagioni, A. Locatelli, C. De Angelis, G. Cerullo, R. Osellame, B. Hecht, L. Duò, F. Ciccacci, M. Finazzi, Mode matching in multiresonant plasmonic nanoantennas for enhanced second harmonic generation, Nat. Nanotechnol. 10 (2015) 412.

[72] G. Grinblat, Y. Li, M.P. Nielsen, R.F. Oulton, S.A. Maier, Degenerate four-wave mixing in a multiresonant germanium nanodisk, ACS Photonics 4 (2017) 2144.

[73] H.K. Tsang, C.S. Wong, T.K. Liang, I.E. Day, S.W. Roberts, A. Harpin, J. Drake, M. Asghari, Optical dispersion, two-photon absorption and self-phase modulation in silicon waveguides at 1.5 μm wavelength, Appl. Phys. Lett. 80 (2002) 416.

[74] K. Ikeda, Y. Shen, Y. Fainman, Enhanced optical nonlinearity in amorphous silicon and its application to waveguide devices, Opt. Express 15 (2007) 17761.

[75] S. Makarov, S. Kudryashov, I. Mukhin, A. Mozharov, V. Milichko, A. Krasnok, P. Belov, Tuning of magnetic optical response in a dielectric nanoparticle by ultrafast photoexcitation of dense electron-hole plasma, Nano Lett. 15 (2015) 6187.

[76] Y. Xu, J. Sun, J. Frantz, M.I. Shalaev, W. Walasik, A. Pandey, J.D. Myers, R.Y. Bekele, A. Tsukernik, J.S. Sanghera, N.M. Litchinitser, Reconfiguring structured light beams using nonlinear metasurfaces, Opt. Express 26 (2018) 30930.

[77] I.Y. Park, S. Kim, J. Choi, D.H. Lee, Y.J. Kim, M.F. Kling, M.I. Stockman, S.W. Kim, Plasmonic generation of ultrashort extreme-ultraviolet light pulses, Nat. Photonics 5 (2011) 677.

[78] S. Ghimire, A.D. Dichiara, E. Sistrunk, P. Agostini, L.F. Dimauro, D.A. Reis, Observation of high-order harmonic generation in a bulk crystal, Nat. Phys. 7 (2011) 138.

[79] H. Liu, C. Guo, G. Vampa, J.L. Zhang, T. Sarmiento, M. Xiao, P.H. Bucksbaum, J. Vučković, S. Fan, D.A. Reis, Enhanced high-harmonic generation from an all-dielectric metasurface, Nat. Phys. 14 (2018) 1006.

[80] C.W. Siders, N.C. Turner, M.C. Downer, A. Babine, A. Stepanov, A.M. Sergeev, Blue-shifted third-harmonic generation and correlated self-guiding during ultrafast barrier suppression ionization of subatmospheric density noble gases, J. Opt. Soc. Am. B 13 (1996) 330.

[81] S.C. Wilks, J.M. Dawson, W.B. Mori, T. Katsouleas, M.E. Jones, Photon accelerator, Phys. Rev. Lett. 62 (1989) 2600.

[82] M.R. Shcherbakov, K. Werner, Z. Fan, N. Talisa, E. Chowdhury, G. Shvets, Photon acceleration and tunable broadband harmonics generation in nonlinear time-dependent metasurfaces, Nat. Commun. 10 (2019) 1345.

[83] A. Weiner, Ultrafast Optics, John Wiley & Sons, 2011.

[84] J. Shah, Ultrafast Spectroscopy of Semiconductors and Semiconductor Nanostructures, 2nd ed., Springer, New York, 1999.

[85] V.R. Almeida, C.A. Barrios, R.R. Panepucci, M. Lipson, All-optical control of light on a silicon chip, Nature 431 (2004) 1081.

[86] U. Strauss, W.W. Rühle, K. Köhler, Auger recombination in intrinsic GaAs, Appl. Phys. Lett. 62 (1993) 55.

[87] A.D. Bristow, J.P.R. Wells, W.H. Fan, A.M. Fox, M.S. Skolnick, D.M. Whittaker, A. Tahraoui, T.F. Krauss, J.S. Roberts, Ultrafast nonlinear response of AlGaAs two-dimensional photonic crystal waveguides, Appl. Phys. Lett. 83 (2003) 851.

[88] M.R. Shcherbakov, S. Liu, V.V. Zubyuk, A. Vaskin, P.P. Vabishchevich, G. Keeler, T. Pertsch, T.V. Dolgova, I. Staude, I. Brener, A.A. Fedyanin, Ultrafast all-optical tuning of direct-gap semiconductor metasurfaces, Nat. Commun. 8 (2017) 17.

[89] P.P. Iyer, N.A. Butakov, J.A. Schuller, Reconfigurable semiconductor phased-array metasurfaces, ACS Photonics 2 (2015) 1077.

[90] D.G. Baranov, S.V. Makarov, V.A. Milichko, S.I. Kudryashov, A.E. Krasnok, P.A. Belov, Nonlinear transient dynamics of photoexcited resonant silicon nanostructures, ACS Photonics 3 (2016) 1546.

[91] A. Rudenko, K. Ladutenko, S. Makarov, T.E. Itina, Photogenerated free carrier-induced symmetry breaking in spherical silicon nanoparticle, Adv. Opt. Mater. 6 (2018) 1701153.

[92] A. Sabbah, D. Riffe, Femtosecond pump–probe reflectivity study of silicon carrier dynamics, Phys. Rev. B 66 (2002) 165217.

[93] B.R. Bennett, R.A. Soref, J.A. Del Alamo, Carrier-induced change in refractive index of InP, GaAs, and InGaAsP, IEEE J. Quantum Electron. 26 (1990) 113.

[94] J. Lee, M. Tymchenko, C. Argyropoulos, P.-Y. Chen, F. Lu, F. Demmerle, G. Boehm, M.-C. Amann, A. Alù, M.A. Belkin, Giant nonlinear response from plasmonic metasurfaces coupled to intersubband transitions, Nature 511 (2014) 65.

[95] O. Wolf, S. Campione, A. Benz, A.P. Ravikumar, S. Liu, T.S. Luk, E.A. Kadlec, E.A. Shaner, J.F. Klem, M.B. Sinclair, I. Brener, Phased-array sources based on nonlinear metamaterial nanocavities, Nat. Commun. 6 (2015) 7667.
[96] L. Zhang, A.M. Agarwal, L.C. Kimerling, J. Michel, Nonlinear Group IV photonics based on silicon and germanium: from near-infrared to mid-infrared, Nanophotonics 3 (2014) 247.
[97] R. Soref, Mid-infrared photonics in silicon and germanium, Nat. Photonics 4 (2010) 495.
[98] D.A. Shilkin, M.R. Shcherbakov, E.V. Lyubin, K.G. Katamadze, O.S. Kudryavtsev, V.S. Sedov, I.I. Vlasov, A.A. Fedyanin, Optical magnetism and fundamental modes of nanodiamonds, ACS Photonics 4 (2017) 1153.
[99] S. Suchalkin, G. Belenky, M. Ermolaev, S. Moon, Y. Jiang, D. Graf, D. Smirnov, B. Laikhtman, L. Shterengas, G. Kipshidze, S.P. Svensson, W.L. Sarney, Engineering Dirac materials: metamorphic $InAs_{1-x}Sb_x/InAs_{1-y}Sb_y$ superlattices with ultralow bandgap, Nano Lett. 18 (2018) 412.
[100] M.G. Barsukova, A.S. Shorokhov, A.I. Musorin, D.N. Neshev, Y.S. Kivshar, A.A. Fedyanin, Magneto-optical response enhanced by Mie resonances in nanoantennas, ACS Photonics 4 (2017) 2390.